

Ocean Aerosols: The Marine Fast-Rotating Shadow-Band Radiometer Network

*M. A. Miller, R. M. Reynolds, and J. J. Bartholomew
Brookhaven National Laboratory
Upton, New York*

Introduction

A network of ship-mounted marine fast-rotating shadow-band radiometers (FRSRs) and broadband radiometers have been deployed over the past four years on several backbone ships, funded jointly by Atmospheric Radiation Measurement (ARM) and National Aeronautic and Space Administration's (NASA's) Sensor Intercomparison and Merger for Biological and Interdisciplinary Studies (SIMBIOS). These radiometers operate continuously and automatically during daylight hours.

There fundamental measurements made by the FRSRs in the network are the direct-normal irradiance and diffuse irradiance in six 10-nm wide channels that span the visible and near-infrared wavelengths (440 nm, 500 nm, 610 nm, 660 nm, 870 nm, and 936 nm) and a broadband channel. These measurements are complemented by broadband solar and infrared irradiance using standard Eppley pyranometers and pyrgeometers. A key enabling technology is the ability to compensate for ship motion without using a stabilized platform. This is accomplished by monitoring the platform motion and heading using advanced sensors, carefully understanding all aspects of the radiometer calibration, particularly the directional characteristics, and applying an appropriate averaging window (2 min) to the 4-s samples. Using this information, software compensation for ship motion can be made.

To date, there are over 100 independent cruises in the FRSR database, ranging in duration from a week to over four months. Data have been collected from all three oceans, as well as during important field campaigns such as Aerosols99, the Indian Ocean Experiment (INDOEX), Nauru99, Aerosol Characterization Experiment (ACE)-Asia, and the Northeast Aerosol Characterization Experiment. The database consists of over 120,000 individual measurements of the radiation budget over the world's oceans, including approximately 40,000 measurements of aerosol optical thickness (AOT) in clear and partly cloudy skies.

The research vessel (R/V) Ronald H. Brown was deployed in the vicinity of East Asia to make aerosol measurements over the ocean during ACE-Asia. Aerosol optical properties and broadband radiation are difficult to measure from ships at sea and specialized instrumentation is required. Instrumentation deployed aboard the Ronald H. Brown included sun photometers of various types: simple, commercially available hand-held units (Microtops; Porter et al. 2001), more sophisticated, research-grade hand-held units (Simbad and SimbadA; Deschamps et al. 2003), and marine FRSRs (Reynolds et al. 2001, Figure 1). All of these sun photometers are passive and measure the narrowband optical thickness, τ_λ , where λ is wavelength, in 10-nm wide channels scattered across the visible and



Figure 1. The portable radiation package with its FRSR.

near-infrared spectrum. Additionally, the FRSRs decompose the irradiance field into direct-normal and Data from the diffuse components, which can be used to retrieve additional information about the nature of the aerosol, as will be demonstrated in this paper. Ancillary broadband radiation measurements were also collected on the R/V Ronald H. Brown, along with a visual assay of sky condition using a motion-compensated, all-sky camera (Figure 2).

Data from sun photometers and other instruments aboard the R/V Ronald H. Brown during ACE-Asia are analyzed in this paper and a “best-estimate” time series of τ_λ is produced. This time series is used to compute a companion time series of α , which is an index describing the wavelength-dependence of the τ_λ typically known as the Angstrom Exponent (Angstrom 1961), as described below. Measurements of τ_λ and calculations of α are combined with a trajectory-based air mass characterization to define a phase space for different aerosol types observed during the ACE-Asia experiment. Similar measurements made in a mid-ocean region during the Aerosols99 experiment are used to place the measurements from ACE-Asia in perspective, and the usefulness of the direct-normal and diffuse irradiance data from the FRSR measurements for validating the over-ocean aerosol models used in various applications is demonstrated.



Figure 2. The Total Sky Imager (TSI).

The Dataset

The R/V Ronald H. Brown left Hawaii on March 15, 2001, and traveled across the North Pacific Ocean at latitude approximately 30-35°N (Figure 3a). The ship subsequently passed into the Philippine Sea, around the southern tip of Japan, through the northern part of the East China Sea, and into the Sea of Japan where it followed a complex trajectory (Figure 3b). During periods when cloud conditions permitted, measurements of τ_λ and α were collected with two Microtops sun photometers, one Simbad and one advanced Simbad (SimbadA) radiometer, and an FRSR. A TSI was used to check the sky condition at the time of the measurement. Based on back trajectories (Draxler 1992), seven relatively distinct aerosol regimes were encountered: marine, polluted, heavily polluted, polluted and dusty, polluted and less dusty, moderately polluted, and polluted by rainy (Figures 3a,b). Aerosol characterization on the basis of back trajectories was not possible for a small portion of the cruise trajectory. As the plot shows, generally polluted and dusty conditions were encountered in the vicinity of Japan, particularly in the Sea of Japan.

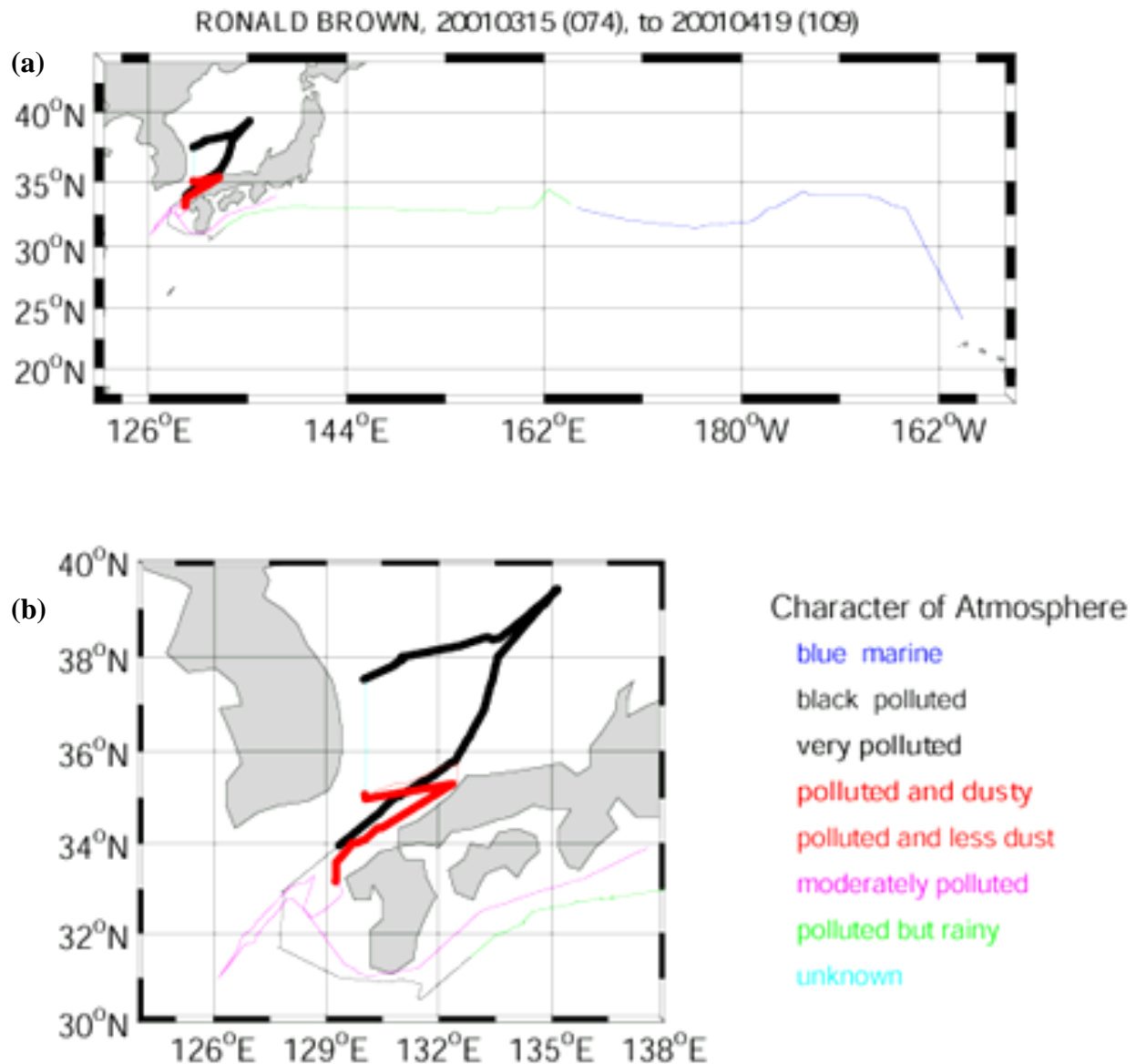


Figure 3. Cruise trajectory of the R/V Ronald H. Brown during ACE-Asia. Latitudes and longitudes are indicated and the cruise trajectory is color coded according to the type of aerosol suggested by a trajectory analysis. The types of aerosol present are given in the accompanying legend.

The application of sun photometry on a ship has the special problem of ship motion. The ship has a periodic rocking motion with a typical period of 5-15 s, and a mean tilt, which can be related to weight distribution, wind forcing, and the directional wave field. It will change slowly over hours or days, and more suddenly if the ship makes an abrupt direction change. Rocking is typically $\pm 1-5^\circ$ on the Ronald H. Brown, while the mean tilt can be $\pm 1-2^\circ$. Each radiometric technique used to measure τ_λ and α on the Ronald H. Brown during ACE-Asia accommodates ship motion in a different manner. The operator stabilizes the hand-held devices, while the FRSR compensates for ship motion by measuring platform motion and compensating for it in post-processing.

The Marine Fast-Rotating Shadow-Band Radiometer

The marine FRSR used on the R/V Ron Brown used a seven-channel (one broadband, six 10-nm narrow-band) silicon-detector-based optical head and a semi-circular occulting arm. It is an operational instrument deployed for long periods and was aboard the R/V Ronald H. Brown two months prior to the beginning of the ACE-Asia campaign. The occulting arm circumscribes a complete rotation centered on the optical head, thereby occulting a band of the sky, with a revisitation period of 6.5 s. The signals from all seven optical channels are sampled rapidly, so the shadow cast by the shadow-band onto the detectors can be recognized and recorded. The mathematics required to compensate for ship motion and compute τ_λ using the FRSR are developed in Reynolds et al. (2001), and uncertainty in the measured values of τ_λ and α is addressed in Miller et al. (2002).

An important application of the FRSR is to provide evaluation data for radiative transfer codes. These codes assume an extra-terrestrial irradiance spectrum at the top of the atmosphere and allow this incoming radiation stream to interact with atmospheric aerosols (or cloud particles) for the purpose of determining the vertical profile of heating in the atmosphere and the quantity of radiation that eventually reaches the surface. There are a number of published extra-terrestrial spectra, sometimes based on satellite radiation measurements. Therefore, it is imperative that the irradiance measurements made by the FRSR be constrained by the same extra-terrestrial irradiance spectrum used in radiation transfer models, or by a close approximation with known biases relative to widely used spectra.

A problem arises when the best-published values for the extra-terrestrial spectral solar irradiance differ by a significant amount (Figure 4). Most of the disagreement in the published spectra occur in the blue-yellow (<600 nm) and in the near infrared (>800 nm) region. The data in Table 1 were obtained by convolving the spectral response functions for the bands in a typical FRSR head with the published solar spectra. The variability in the estimates in Table 1 reflects a combination of instrument uncertainty and variation in the solar output spectrum. The values for 415 nm have a difference of 4.6% over the range shown, for 500 nm 2.3%, for 615 nm 2.6%, for 670 nm 1.9% and for 870 nm 7.3%. The measurements of the extra-terrestrial solar spectrum made from space (Colina et al. 1996; Thuillier et al. 1998; and Thuillier et al. 2002) are considered to be the best. From these, the Thuillier et al. (2002) values are chosen as the reference spectrum for the FRSR because the data were collected during four different missions, thereby making this the largest and most comprehensive datasets to date.

As previously mentioned, $I_{\lambda,0}$ for sun photometers are generally determined through the Langley technique. As discussed below, however, the Langley technique cannot be used to calibrate FRSRs at sea due to orientation uncertainty. Langley plots for the FRSR must be performed on land. Langley calibrations of FRSRs on land at Mauna Loa, Hawaii; Mt. Lemmon, Arizona; and on the roof of Building 490D at Brookhaven National Laboratory, Upton, New York; generally provide values of $I_{\lambda,0}$ that agree within 1-2% of the Thuillier et al. (2002) values. Accordingly, the $I_{\lambda,0}$'s used to process FRSR data are derived by convolving the instrument bandpass with the Thuillier et al. (2002) values, rather than through frequent Langley analyses, as would be the case on land. The instrument gain change is estimated using pre- and post-cruise calibrations and adjusted in the data in post-processing, in an attempt to maintain a calibration consistent with the Thuillier et al. (2002) values. At sea, AOT measurements are also compared with hand-held sunphotometer data (when it is available) to track drift and FRSRs are calibrated in a laboratory as frequently as possible. For the purpose of linking FRSR

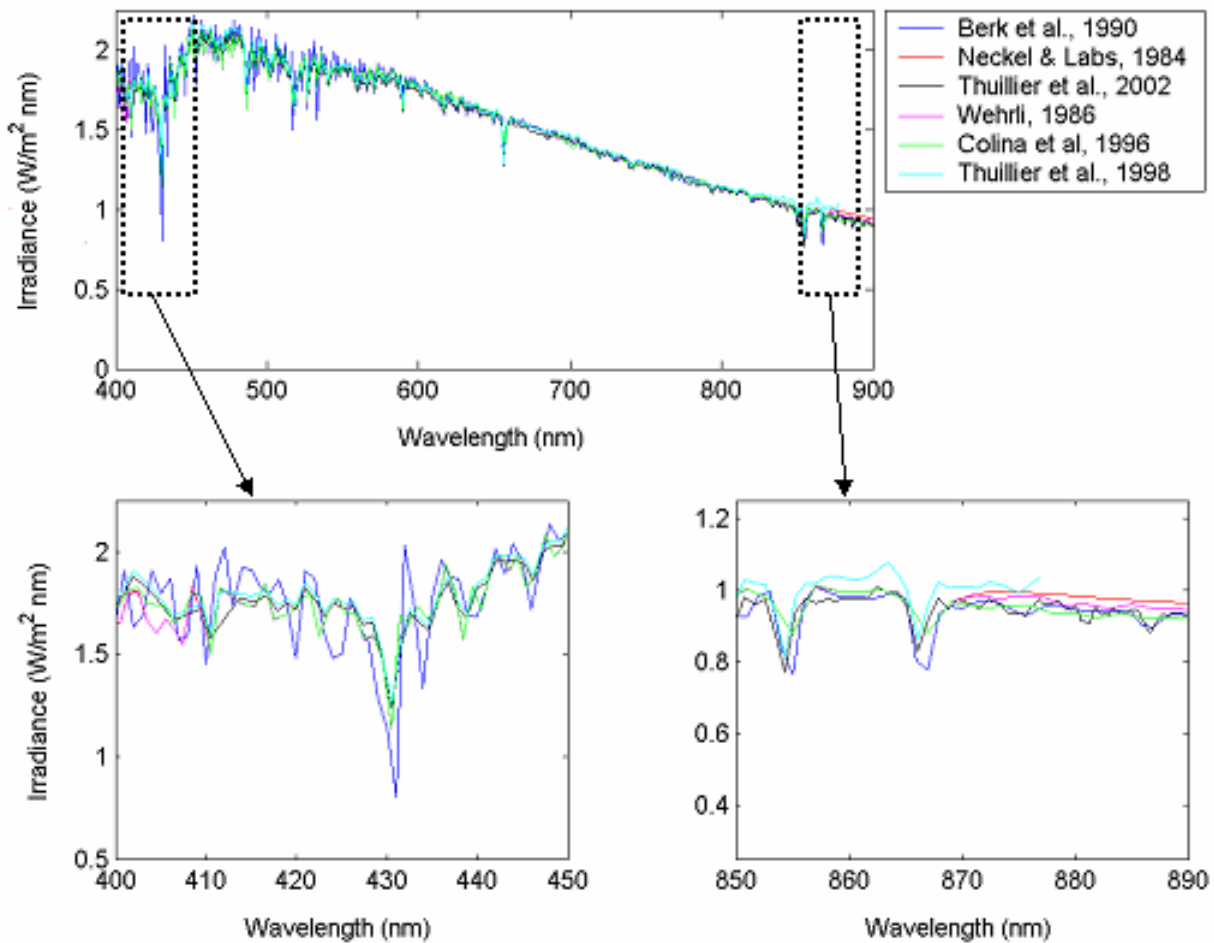


Figure 4. A comparison of six different extra-terrestrial solar spectral irradiances ($W m^{-2}$) as a function of wavelength. The lower illustrations are high resolution plots of the 400-450 nm (violet-blue) and 850-890 nm (near-infrared) regions of the spectrum.

Table 1. Data obtained by convolving the spectral response functions for the bands in a typical FRSR head with the published solar spectra.

$\lambda(\text{nm})$	Mean	N-L84	W86	B90	C96	T98	T02
415	1.753	-1.03	-1.14	3.31	-0.80	1.14	-1.25
500	1.952	-0.51	-0.67	-0.20	-0.46	1.04	0.26
615	1.700	0.76	0.65	-0.06	0.76	-0.47	-1.82
670	1.526	0.20	0.07	0.59	0.20	0.20	-1.31
870	0.962	0.52	0.10	-2.91	-1.04	4.16	-1.04
940	0.826	5.21	-2.42	-0.36	-0.24	-2.42	-0.12

irradiance to radiation codes, it is appropriate to assume on the basis of experience and the values in Table 1, that the uncertainty in the absolute extra-terrestrial calibration for a typical FRSR is approximately 1.5%, assuming that the Thuillier et al. (2002) values are accurate. Because there is significant uncertainty in the solar reference spectra itself, this uncertainty could be significantly larger, particularly at 870 nm, whereupon later calculations show results for uncertainties of 1.5% and 3.0% for guidance.

Calculations of $\sigma_{\tau_{\lambda A}}$ for several different situations were performed (Figure 5). The first experiment shows $\sigma_{\tau_{\lambda A}}$ for optimal FRSR operating conditions, when the uncertainty in the extra-terrestrial irradiance is 1.5% and the gain uncertainty is 2%. Calculations for $0, \pm 2,$ and $\pm 8^\circ$ were made, representing the envelopes of typical wave motion, mean tilt, and no motion. The envelope of $\sigma_{\tau_{\lambda A}}$ is quite narrow through solar zenith angles (SZAs) of 60° , but degrades rapidly at low SZAs in the $\pm 8^\circ$ case (typical wave motion). Conversely, 2° uncertainty in the mean tilt produces a negligible

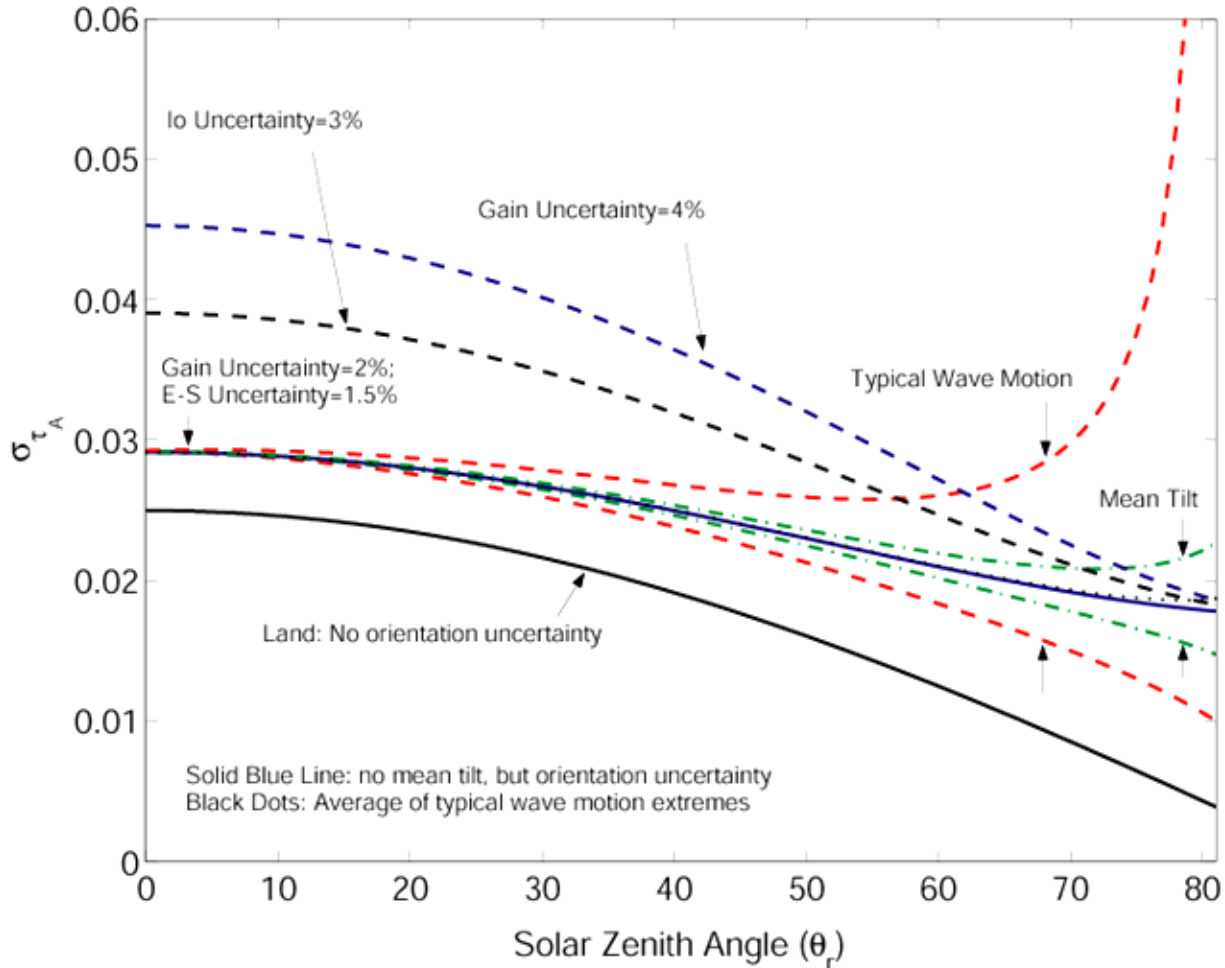


Figure 5. The uncertainty in the FRSR measurement of AOT, $\tau_{\lambda A}$, as a function of SZA, θ_e . Under typical circumstances, the uncertainty in instrument gain is 2%, the uncertainty in the edge-shadow voltage measurement is 1.5%, and the uncertainty in the extra-terrestrial irradiance is 1.5% (family of curves indicated on plot). The orientation uncertainty envelopes for typical wave motion (red-dashed lines; roll or pitch angles of $\pm 8^\circ$) and typical mean tilt (green-dashed lines; roll or pitch angles of $\pm 2^\circ$) are plotted. The black dots result from averaging the typical wave motion ($\pm 8^\circ$), which is a random variable; this exercise demonstrates that averaging these random waves essentially causes no bias due to the cosine response of the radiometer. The blue dashed line represents a doubling of the gain uncertainty to 4% (edge-shadow voltage uncertainty remains 1.5%). The black dashed line represents a doubling of the uncertainty in the extra-terrestrial irradiance to 3%.

effect on $\sigma_{\tau_{\lambda A}}$ as compared to the no motion case. Averaging the $\pm 8^\circ$ typical wave motion extremes provides an estimate of the impact of averaging the individual sweeps taken a 6.5 s intervals over 2 min (black dots); as anticipated, this calculation shows that the averaging approximates the “no-motion” case, reinforcing the notion that averaging the typical wave motions to compute the mean tilt should produce acceptable results. The mean tilt on ships on which the FRSR is currently deployed is less than 2° , which suggests $\tau_{\lambda A}$ can be measured with an FRSR to an accuracy of 0.03 or better under most circumstances, assuming that the gain uncertainties are 2° and the absolute accuracy of $I_{\lambda 0}$ is known to 1.5%.

An interesting experiment is to calculate the uncertainty of a land-based FRSR whose orientation is perfectly known and gain uncertainty is 2% and $I_{\lambda 0}$ uncertainty is 1.5%. This calculation (black line on Figure 5) shows that the land-based unit benefits from the “lever-arm” property of the Langley technique, which allows $\sigma_{\tau_{\lambda A}}$ to be estimated with increasing accuracy as the SZA increases. When an FRSR is mounted on a ship, the advantages of the “lever-arm” are essentially offset by the increasing orientation uncertainty at high SZAs; this produces a nearly constant uncertainty in $\tau_{\lambda A}$ ($\sigma_{\tau_{\lambda A}}$) as a function of the SZA. Moreover, this offsetting effect suggests that the Langley technique itself cannot be performed under most conditions at sea. Thus, FRSRs deployed on ships must be calibrated on land.

Two additional experiments are to degrade the $I_{\lambda 0}$ uncertainty to 3.0% (dashed black line on Figure 5), suggesting a poor knowledge of the extra-terrestrial spectrum, and the gain uncertainty to 4% (dashed blue line), suggesting significant drift over time. Either of these conditions can add 0.01-0.02 to $\sigma_{\tau_{\lambda A}}$.

An increase in gain uncertainty is a much more likely scenario for an FRSR exposed to the elements during long deployments. It should be reinforced that the absolute uncertainty $I_{\lambda 0}$ is a function of inaccurate specification of the reference spectrum and the ability to perform an accurate Langley calibration, while gain uncertainty is the result of degrading hardware components, such as interference filters and the diffuser material.

Companion experiments to calculate the uncertainty in the two-wavelength Ångström exponent, α , were performed (Figure 6). Conditions were varied from clean ($\tau_{\lambda A} = 0.05$, $\alpha = 0$) to polluted ($\tau_{\lambda A} = 0.2$, $\alpha = 1$) air masses. The experiments demonstrate that the uncertainty in measuring α ($\sigma_{\lambda A}$) is a strong function of $\tau_{\lambda A}$ and α . As in previous experiments, the envelope of uncertainty for typical wave motion ($\pm 8^\circ$) shows that (red dashed lines) σ_{α} is not particularly sensitive to the wave motion until the SZA exceeds 60° . The land versus ocean experiment once again reflects the fact that the “lever-arm” effect is offset by uncertainty in the position of the FRSR on a moving ship, producing a $\tau_{\lambda A}$ that is nearly independent of the SZA. Experiments with degradation in the uncertainty of knowledge of $I_{\lambda 0}$ (black dashed line) and with gain (blue dashed line) again show sensitivity to gain uncertainty.

The most striking aspect of the Ångström exponent uncertainty is that it is so much greater in clean air masses ($\tau_{\lambda A} = 0.05$, $\alpha = 0$), where it is approximately 0.7 in contrast to the polluted case, which is an order of magnitude lower. The plot also shows that this situation exists for land-based units. On the surface, this characteristic appears to be advantageous, since most applications of the FRSR involve

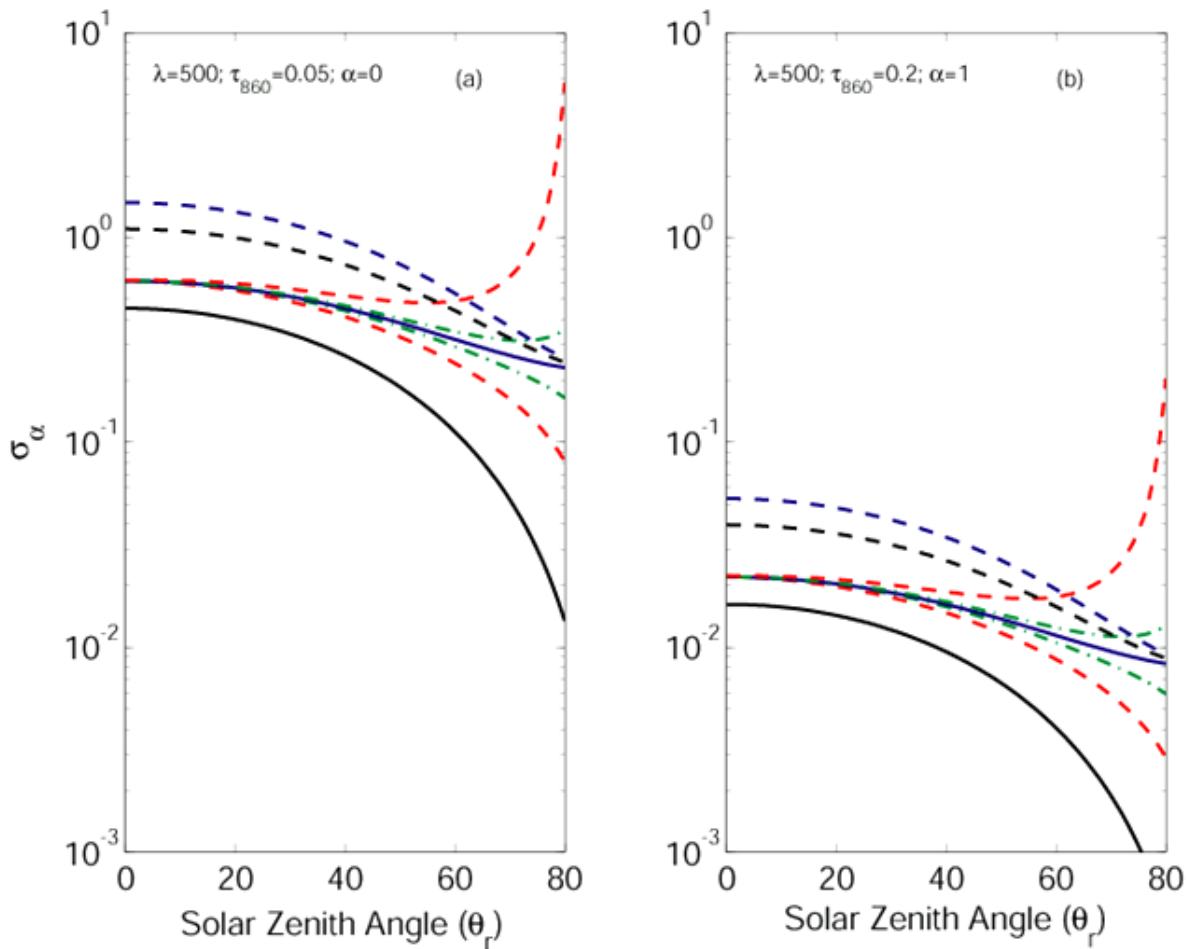


Figure 6. Same as in Figure 5, but for Ångström exponent. (a) Plots of σ_α versus θ_e for a clean maritime air mass ($\tau_{\lambda A} = 0.05$, $\alpha = 0$) and (b) for a polluted air mass with ($\tau_{\lambda A} = 0.2$, $\alpha = 1$).

polluted air; the downside is that it seems that the FRSR is unable to accurately measure the wavelength-dependent characteristics of marine aerosol (sea-salt). While these aerosols contribute minimally to the local radiation budget, their spatial coverage over the world's oceans suggests that they could be important in the global radiation budget.

The extra-terrestrial irradiances used to process FRSR data for the ACE-Asia campaign are derived by convolving the instrument band-pass with the Thuillier et al. (2002) values, rather than through frequent Langley analyses, as would be the case on land. The instrument gain is monitored by comparing the broadband channel with the more stable broadband measurements from an Eppley pyranometer mounted on the FRSR platform. The gains are adjusted in the data in post-processing, in an attempt to maintain a calibration consistent with the Thuillier et al. (2002) values.

The FRSR differs from hand-held sun photometers because it collects data continuously. Because the marine boundary layer is particularly cloudy environment, measurements of $\tau_{\lambda A}$ are often contaminated by $\tau_{\lambda C}$, the optical thickness of clouds. To a large extent, filtering of observations that contain cloud

(cloud contamination) from those that do not is done subjectively by the operator in the case of the hand-held sun photometers. While this method is fairly effective, it is not foolproof, and data from hand-held devices must still be screened to remove remaining cloud effects. In contrast, the FRSR collects data continuously, which dictates that cloud contamination will be naturally included in the data record since there is no initial subjective filtering. Therefore, an automatic cloud-filtering algorithm is an essential component of the instrument.

The conceptual foundation of the cloud filter that is used to process the FRSR data in this paper comes from the differing levels of variability observed in the two signals, $\tau_{\lambda A} + \tau_{\lambda C}$ and $\tau_{\lambda A}$. Broken cloud fields show large variations in τ_{λ} as clouds drift across the solar disk. In contrast, $\tau_{\lambda A}$ is reasonably constant over periods of an hour or two due to the time scales of the physical processes that typically modulate changes in the aerosol load. Each individual observation is considered in the cloud filter, and the scatter between neighboring observations is a key metric that is used in the filtering scheme.

In contrast to the hand-held sun photometers, the FRSR samples at a 4-s rate and measurements are averaged over a 2-min period. Conceptually, this amounts to an attempt to average out high frequency pitch and roll motions, leaving only the mean tilts. These tilts are subsequently removed from the data by measuring the exact platform motion during the 2-min period, and compensating in software.

Results

The geometric daily mean of $\tau_{\lambda A}$ was computed for the three overlapping bands (500, 670, 870 nm) from the consensus time series. The geometric mean, rather than the arithmetic mean, is used because statistics of $\tau_{\lambda A}$ from long-term studies show a lognormal distribution (O'Neill et al. 2000; Ignatov and Stowe 2001). Statistics were computed for the consensus time series for a 1-h window around local noon (hereafter referred to as the noon consensus statistics), which is traditionally the satellite overpass time, and for a 4-h window around local noon. Although there are some periods when the daily and noon statistics diverged slightly, in most cases there was good agreement, suggesting that the aerosol conditions were relatively homogeneous through the day (Figure 7). Therefore, only the 1-h consensus statistics about local noon are analyzed.

Cross-referencing measurements of $\tau_{\lambda A}$ at 870-nm with the chemical trajectory analysis demonstrates the correspondence between air mass trajectory and $\tau_{\lambda A}$ (Figure 7a). Before Julian day 93, values of $\tau_{\lambda A}$ are generally less than 0.1 and have standard deviations on the order of ~ 0.03 , which is expected due to 0.02-0.03 measurement uncertainties. On Julian day 94, as the ship rounds the southern tip of Japan, values of $\tau_{\lambda A}$ begin a steady increase culminating in two separate peaks in which the aerosol load has a profound impact on the aerosol optical properties. The geometric mean value of $\tau_{\lambda A}$ is exceptionally large on days 99 and 100, exceeding 0.8 at 500 nm, and 0.6 at 670-nm and 870-nm on the latter day (Figures 7b-d). This is one of the largest values of $\tau_{\lambda A}$ observed at sea with the FRSR after some 40 separate deployments over the world's oceans. The variability of $\tau_{\lambda A}$ is noticeably larger at 870 nm (near-infrared) than at 500 nm (blue-green). This observation suggests that in the polluted regions the local variations in α are mostly modulated by changing conditions in the near-infrared band.

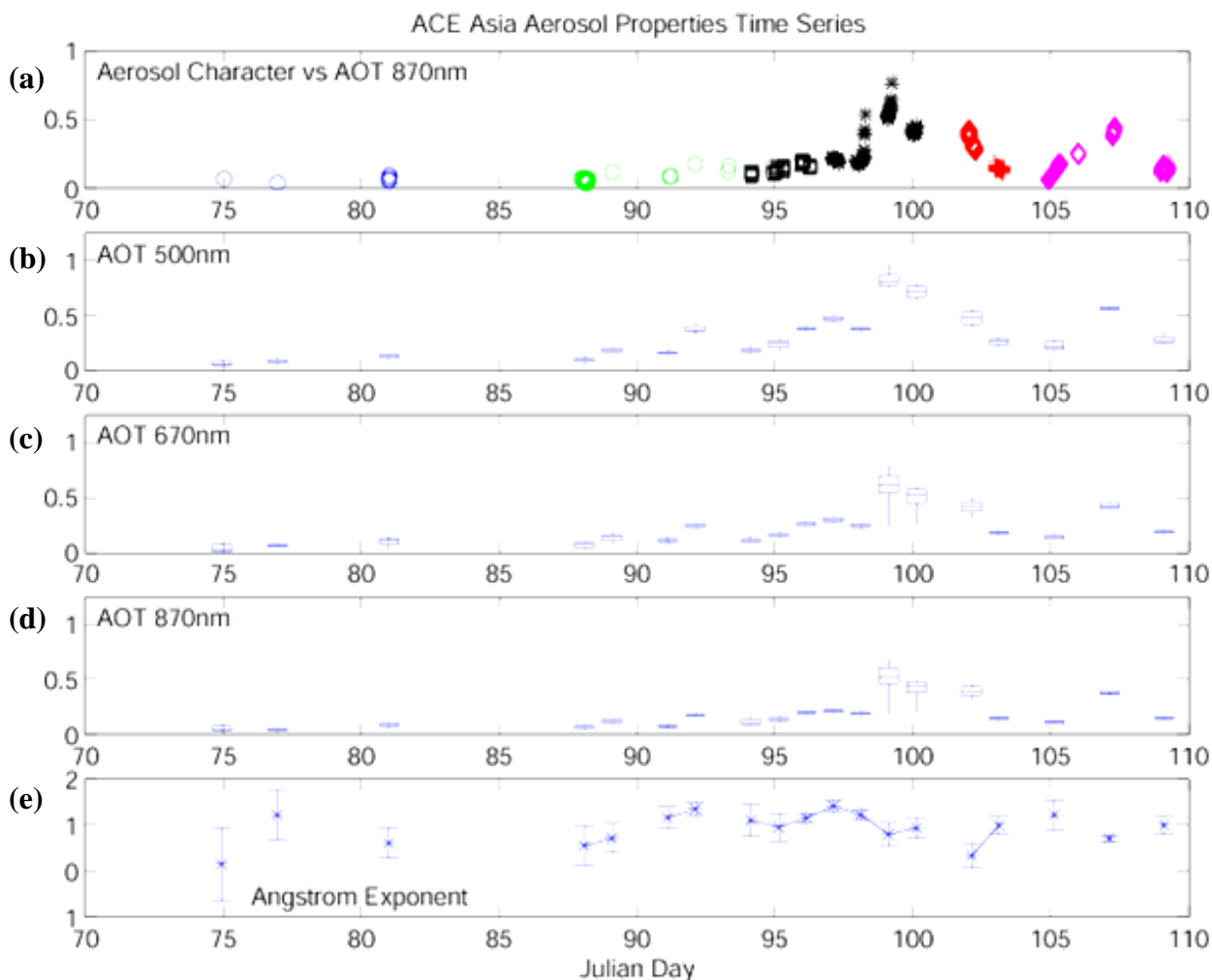


Figure 7. (a) Plot of AOT at 870 nm classified by trajectory-based air mass type. The different air masses are plotted according to the color codes in Figure 1 and with different symbols; (b) Time series of the geometric statistics of cloud-filtered AOT at 500 nm for a 1-h window around local noon. The whisker plots show the geometric median (center bar), the geometric standard deviations (upper and lower bounds of box), and the lines above and below represent the maximum and minimum observed values; (c) as in (b) but for 670 nm; (d) as in (b), but for 870 nm; (e) Angstrom exponent for the experiment period.

The time series shows that maximum values of α do not correspond with the maximum values of $\tau_{\lambda A}$ (Figures 7a-e). In fact, there seems to be an inverse relationship between the two variables when the ship is traversing the polluted areas. Moreover, the maximum variability in the value of $\tau_{\lambda A}$ is found during the two days with the highest values of $\tau_{\lambda A}$, although the motion of the ship through the pollution plume complicates interpretation. One possibility is that mixing processes occurring downwind of the plume are not yet complete, thereby producing changeable aerosol optical conditions.

To place the ACE-Asia R/V Ron Brown in context, it can be compared to similar FRSR observations collected during the Aerosols99 experiment, which followed a north-south trajectory across the Atlantic from North Carolina to Cape Town, South Africa (Figure 7; Voss et al. 2001). Trajectory analysis for

this cruise discretely identified four different regimes: biomass burning, dust, Northern Hemisphere clean, and Southern Hemisphere clean. No indication as to the presence of precipitation is given for the Aerosols99 experiment data. When the Aerosols99 data are added, the phase space of $\tau_{\lambda A}$ and α is better defined for a wider range of aerosol conditions. With the exception of the periods in transit to the region around Japan, the ACE-Asia data are largely representative of a coastal environment, which dictates rather close proximity to the sources. Conversely, the Aerosols99 data are far removed from sources, so the aerosols within the air mass have likely evolved in transit. Thus, the extremes observed in the Aerosols99 data represent highly evolved aerosol states: air that has been nearly completely cleansed of continental impacts (Northern and Southern Hemisphere clean) and dust and biomass-burning plumes that have been highly modified. As will be discussed in the section that follows, these two datasets (Figure 8) present a view of aerosol evolution.

The Northern and Southern Hemisphere clean air masses, which are assumed to consist primarily of sea-salt aerosol, have smaller values of α than the polluted but rainy air masses observed during ACE-Asia. The small and occasionally negative α 's suggest that relatively larger aerosol particles are present than in the polluted, but rainy, cases during ACE-Asia. The suggestion is that the polluted air mass with rain observed during ACE-Asia is not yet completely cleansed of pollution; it's in an intermediate phase.

The dust and biomass burning aerosols observed during Aerosols99 occupy a region of the phase space that is devoid of observations from ACE-Asia (Figure 8). Specifically, the biomass-burning plume has generally smaller values of α than the polluted air mass observed during ACE-Asia, which is thought to be associated with urban effluents. This suggests that the aerosol particles that comprise the biomass-burning plume are generally larger in size than those in the urban effluent plume. The Saharan dust observed during Aerosols99 also has smaller α 's than the mixtures observed during ACE-Asia, again suggesting larger particles.

The diffuse-to-direct ratio time series (Figure 9) appears similar to the time series of $\tau_{\lambda A}$; this is expected because $\tau_{\lambda A}$ is derived from the direct-normal radiation component. The ratio of diffuse-to-direct irradiance in the three bands (Figures 9a-c) shows that the most noticeable change in this ratio occurs in the 500-nm band, which is blue-green to the eye. Small aerosol particles scatter more efficiently in the violet and blue wavelength bands, so increasing loads of these small particles enhances multiple scattering, thereby leading to an increase in diffuse irradiance, particularly in the violet and blue (400-500 nm). Changes in the other bands are less pronounced, especially in the near-infrared region (870-nm), mainly because small aerosol particles do not scatter efficiently in that band. When the air mass becomes highly polluted (days 99-102); however, there is a noticeable change in the near-infrared band. This change suggests that the scattering characteristics of the aerosol particles that comprise the air mass are changing in a fundamental way such that proportionately more near-infrared radiation is being scattered. Inspection of data from the TSI illustrates the two extremes in sky condition encountered during the cruise: a clean, maritime air mass over the Northern Pacific Ocean (Figure 10a) and a highly polluted air mass over the Sea of Japan (Figure 10b). Note the extremely blue sky and modest whitening at the horizon in the clean air mass (Figure 10a) as opposed to the polluted air mass (Figure 10b). Note the brownish color of the horizon in the polluted air mass and that the entire sky appears to be dull and whitened. The reduction in total irradiance between the two air masses is graphically illustrated by comparing the brightness of the ship's superstructure in the two images. The solar aureole, which is the

faintly colored luminous ring that surrounds the sun's disk through the haze, is significantly larger and brighter in the polluted air mass.

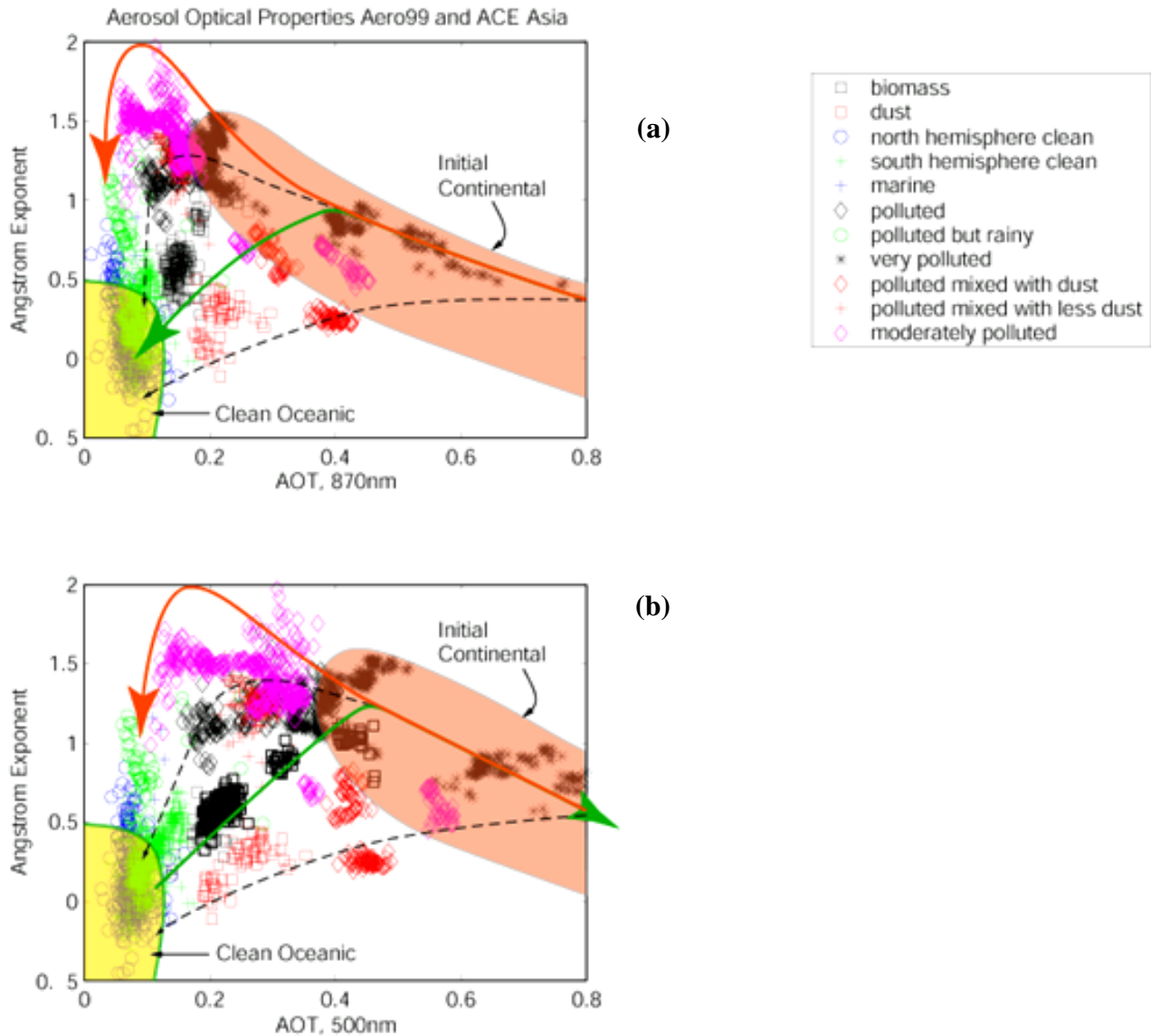


Figure 8. (a) A plot of versus for the R/V Ronald H. Brown during ACE-Asia and Aerosols99 with data classified according to air mass type via trajectory analysis. The different air mass types are shown on the legend; (b) as in (a), but for versus. The orange hatched region shows the aerosol optical properties qualitatively described as “initial continental” and the yellow hatched area shows those that can be described as “clean oceanic.” The red arrow shows the trajectory through, phase space that would theoretically be followed in time if the aerosols embedded within the air mass experienced only dry deposition. The green arrow shows the theoretical trajectory of aerosols experiencing wet deposition.

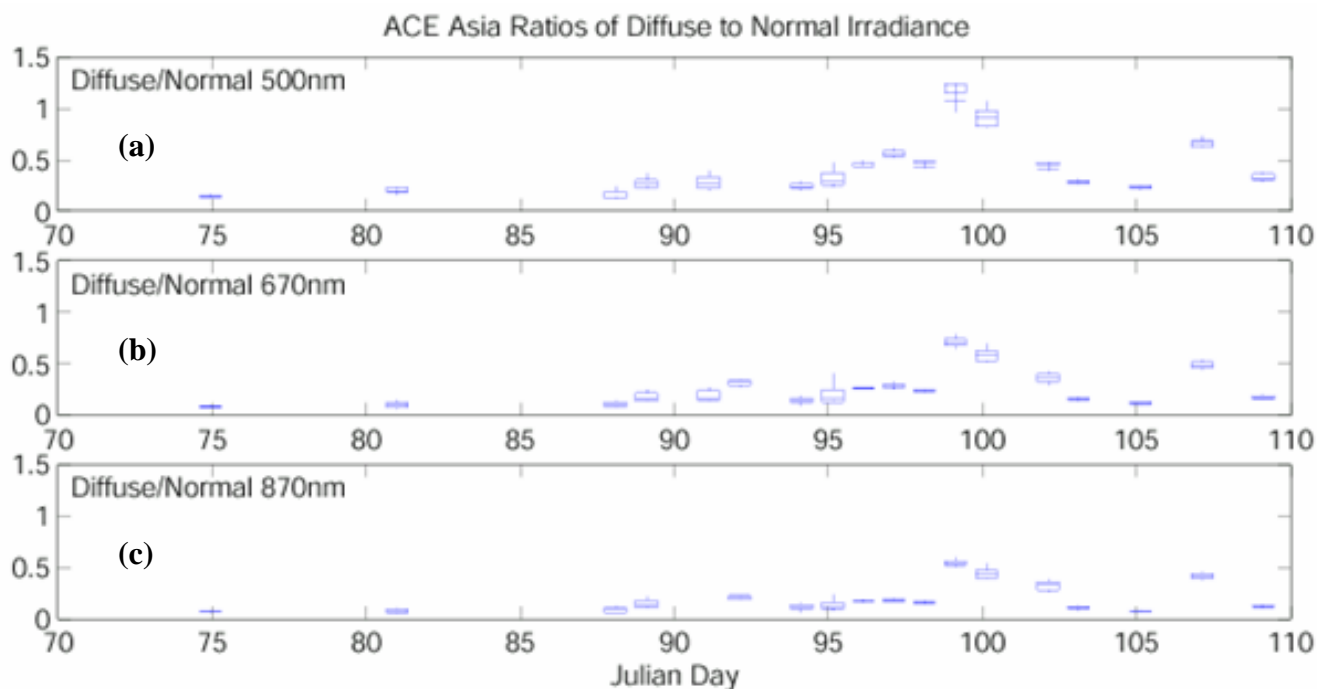


Figure 9. Plots of the ratio of diffuse irradiance to direct-normal irradiance from the FRSR during ACE-Asia for the 1-h window around local noon. The whisker plots show the geometric median (center bar), the geometric standard deviations (upper and lower bounds of box), and the lines above and below represent the maximum and minimum observed values; (a) 500 nm, (b) 670 nm, and (c) 870 nm.

The contrasting sky conditions shown in the TSI data are quantified using the diffuse-to-direct irradiance ratio measured by the FRSR. The enlarged solar aureole in highly polluted air masses (and when thin cirrus is present) necessitates an adjustment in the FRSR sweep-level processing (Miller et al. 2002). This is because the direct beam irradiance is computed using the difference between the shadow irradiance and the edge irradiance, which is the irradiance just before the occulting band reaches the edge of the solar disk (Reynolds et al. 2001). When an air mass is clean and the solar aureole is minimal, well-defined edge-shadow irradiances can be determined from the individual sweeps within the 2-min data collection window (Figure 10a). The variability from sweep-to-sweep is caused by ship motion (Miller et al. 2002). In contrast, the solar aureole is much less defined in the polluted air mass. This situation requires that a non-linear, curve-fitting scheme be employed to determine the edge irradiance. Most importantly, the state-of-the-sky as inferred from individual sweep data from the FRSR and visual evidence from the TSI clearly suggests that multiple scattering cannot be ignored in this highly polluted environment.

Corresponding Author

Mark A. Miller, miller@bnl.gov, (631) 344-2958

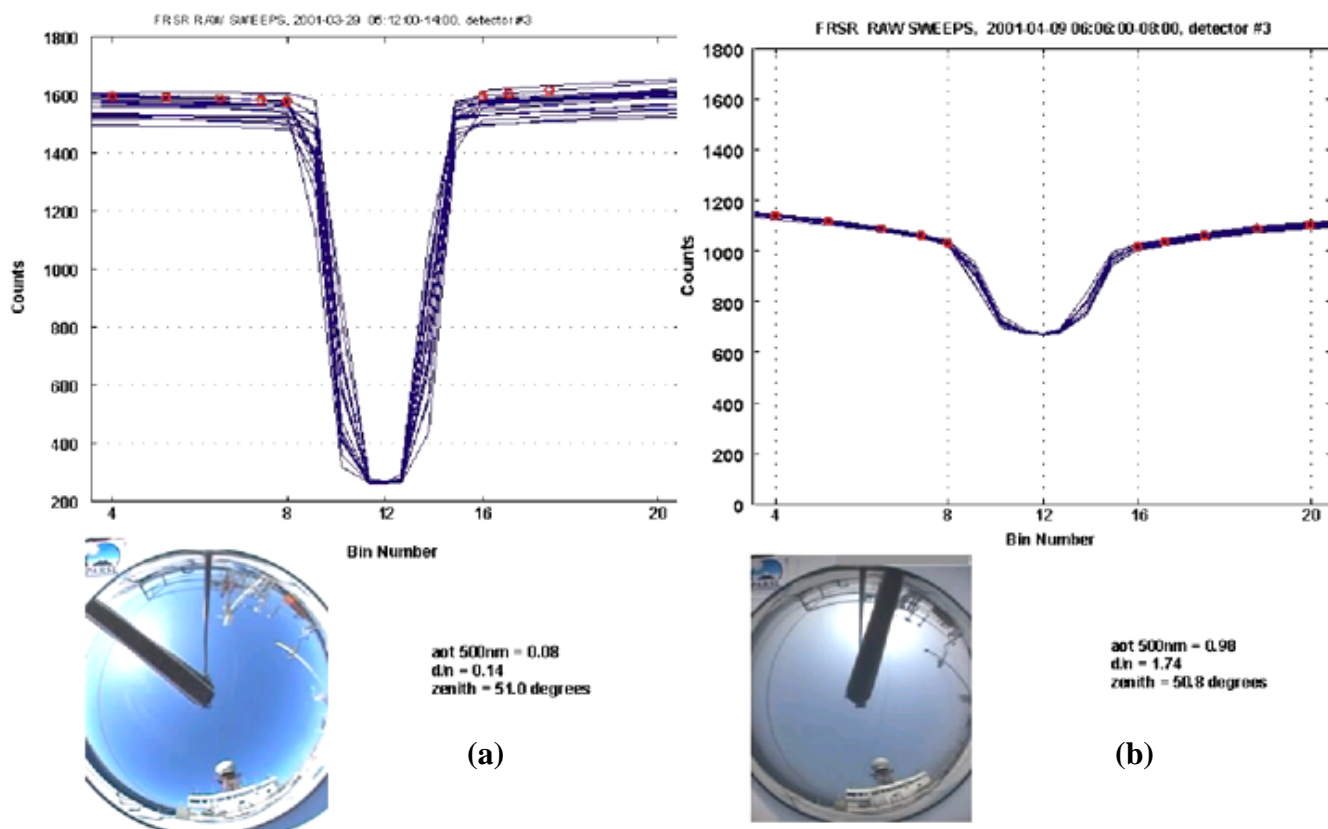


Figure 10. (a) A plot of the time series of voltage counts from the FRSR for each sweep that passed quality control during a 2-min sampling window. These individual sweeps are used to determine the direct-normal irradiance. The red circles represent the voltages selected by the FRSR processing as representative of the “edge” voltage (Reynolds et al. 2001; Miller et al. 2003). A visible sky images from the TSI for one of the individual sweeps from (a) the Northern Pacific Ocean in a clean air mass (AOT = 0.08 at 500 nm) and (b) the polluted air mass above the Sea of Japan (AOT = 0.98 at 500 nm).

References

- Ångström, A., 1961: Techniques for determining the turbidity of the atmosphere. *Tellus*, XIII, 214-223.
- Berk, A., L. S. Bernstein, and D. C. Robertson, 1990: MODTRAN: A Moderate Resolution Model for LOWTRAN7, Tech. Report GL-TR-90-0122, p.44, Geophysical Directorate Phillips Laboratory, Hanscom AFB, Massachusetts.
- Colina, R., C. Bohlin, and F. Castelli, 1996: The 0.12-2.5 micrometer absolute flux distribution of the sun for comparison with solar analog stars. *Astronomy Journal*, **112**, 307-315.
- Deschamps P.-Y., P. Lecomte, C. Verwaerde, B. Fougnie, and R. Frouin, 2002: SIMBAD: A field radiometer for satellite ocean-color validation. *Applied Optics*, submitted.

Draxler, R. R., 1992: *Hybrid Single-Particle Lagrangian Integrated Trajectories (HY-SPLIT): Version 3.0, Users Guide and Model Description*, Tech. Rep. ERL ARL-195, National Oceanic and Atmospheric Administration, Silver Springs, Maryland.

Ignatov, A., and L. Stowe, 2001: Aerosol Retrievals from Individual AVHRR Channels. Part II: Quality Control, Probability Distribution Functions, Information Content, and Consistency Checks of Retrievals. *J. Atmos. Science*, **59**, 335-362.

Long, C. N., D. L. Slater, and T. Tooman, 2001: *Total Sky Imager Model 880 Status and Testing Results*, U.S. Department of Energy Atmospheric Radiation Measurement Program Technical Report, TR-006, p. 36.

Miller, M. A., M. J. Bartholomew, and R. M. Reynolds, 2003: The accuracy of marine shadow-band measurements of aerosol optical thickness and Angstrom exponent. *J. Atmos. Ocean. Tech.*, submitted.

O'Neill, N. T., A. Ignatov, B. Holben, and T. Eck, 2000: The log-normal distribution as a reference for reporting aerosol optical depth statistics; empirical tests using multi-year, multi-site AERONET sun photometer data. *Geophys. Res. Lett.*, **27**, 3333-3336.

Porter, J. N., M. A. Miller, C. Motell, and C. Pietras, 2001: Use of hand-held sun photometers for measurements of aerosol optical thickness at sea. *J. Atmos. Ocean. Tech.*, **18**, 765-774.

Reynolds, M. R., M. A. Miller, and M. J. Bartholomew, 2001: A fast-rotating, spectral shadowband radiometer for marine applications. *J. Atmos. Ocean. Tech.*, **18**(2), 200-214

Thuillier, G., M. Herse, P. C. Simon, D. Labs, H. Mandel, D. Gillotay, and T. Foujols, 2002: The solar spectral irradiance from 200 to 2400 nm as measured by the SOLSPEC spectrometer from the ATLAS 1-2-3 and EURECA missions, *Solar Physics*.

Thuiller, G., M. Herse, P. C. Simon, D. Labs, H. Mandel, and D. Gillotay, 1998: Observations of the solar spectral irradiance from 200 nm to 870 nm during the ATLAS 1 and ATLAS 2 missions by the SOLSPEC spectrometer. *Metrologia*, **35**, 689-695.

Thuillier, G., M. Hersé, P. C. Simon, D. Labs, H. Mandel, D. Gillotay, and T. Foujols, 2002. The solar spectral irradiance from 200 to 2400 nm as measured by the SOLSPEC spectrometer from the ATLAS 1-2-3 and EURECA missions. *Solar Physics*, to be submitted.

Voss, K. J., E. J. Welton, P. K. Quinn, R. Frouin, M. A. Miller, and R. M. Reynolds, 2001: Aerosol optical depth measurements during the Aerosols99 experiment. *J. Geophys. Research*, **106**, 20,811-20,820.

Wehril, C., 1986: Spectral solar irradiance data, World Climate Research Program (WRCP) Publication Series No. 7, WMO ITD No. 149, 119-126.